Modelling the seismic performance of rooted slopes from individual root–soil interaction to global slope behaviour

Liang, T.; Knappett, J. A.; Duckett, N.

Published in:
Géotechnique

DOI:
10.1680/jgeot.14.P.207

Publication date:
2015

Document Version
Publisher's PDF, also known as Version of record

Liang, T. *et al.* (2015). *Géotechnique* **65**, No. 12, 995–1009 [http://dx.doi.org/10.1680/geot.14.P.207]

Modelling the seismic performance of rooted slopes from individual root–soil interaction to global slope behaviour

T. LIANG*, J. A. KNAPPETT* and N. DUCKETT†

Many natural and man-made slopes are planted with vegetation, and it is known that this can increase the stability of slopes under static conditions. There is anecdotal evidence that vegetated slopes also perform better than fallow slopes during earthquakes. However, the study of the dynamic behaviour of slopes planted with species having dichotomous ('woody') roots is relatively rare owing to the extreme expense and difficulty involved in conducting full-scale dynamic testing on shrubs and trees. In this paper, dynamic centrifuge testing and supporting numerical modelling have been conducted to study this problem. In the centrifuge modelling, ABS plastic rods are used to simulate repeatably the mechanical properties of real roots. The numerical modelling work consisted of two parts. First, a computationally-efficient beam-on-non-linear-Winkler-foundation (BNWF) model using existing p–y formulations from piling engineering was employed to produce a macro-element describing the individual root and soil interaction both pre- and post-failure. By adding contributions from the different root analogues of different diameters, smeared continuum properties were derived that could be included in a fully dynamic, plane-strain continuum, finite-element model in a straightforward way. The BNWF approach was validated against large direct shear tests having stress conditions simulating those in the centrifuge at different potential slip plane depths. The conversion to smeared properties for global time-history analysis of the slope was validated by comparing the continuum finite-element results with the centrifuge test data in terms of both the dynamic response and permanent deformations at the crest, and these demonstrated good agreement. Owing to the simplicity of the BNWF approach and its ability to consider variable root geometries and properties, along with variation of soil properties with depth, it is suggested that the validated approach described will be useful in linking individual root–soil interaction characteristics (root strength and stiffness, diameter variation, root spacing and so on) to global slope behaviour.

KEYWORDS: centrifuge modelling; earthquakes; finite-element modelling; numerical modelling; slopes; vegetation

INTRODUCTION

Vegetation (grasses, shrubs and trees), as an effective and environmentally friendly approach to improving slope stability, improves slope stability mainly through direct mechanical reinforcement of soil and by modifying groundwater conditions by means of evapotranspiration. The net effect of both of these mechanisms is an increase in shear strength within a defined zone around the roots, although only the mechanical effect is present at all times; the hydrological effects potentially disappear following heavy rain. In terms of the direct mechanical effect, many studies have been performed to quantify the increase in soil strength due to roots. Analytical models (e.g. Waldron, 1977; Pollen & Simon, 2005) and numerical models (e.g. Van Beek *et al.*, 2005; Lin *et al.*, 2010; Mickovski *et al.*, 2011) based around full continuum finite-element (FE) modelling of small soil–root zones have been introduced and validated against laboratory and in situ shear tests (Wu, 2013). A fibre breakage model, which permits the use of a transitioning discontinuous function in FE modelling, was also developed to simulate the progressive tensile failure of roots, and evaluate the behaviour of a vegetated slope (Tiwari *et al.*, 2013). Despite such attention, the majority of this work has focused on static cases. Relatively few, if any, studies have been performed to investigate the dynamic performance of vegetated slopes during earthquakes, which are a perennial threat to slope stability, in contrast to other more traditional reinforcing elements within slopes such as geosynthetic layers (or 'reinforced earth', e.g. Ausilio *et al.* (2000)) and piles (e.g. Kourkoulis *et al.*, 2011). Geotechnical centrifuge testing using both real plants and simple straight root analogues was reported by Sonnenberg *et al.* (2010) and Sonnenberg *et al.* (2011) for the case of a static rise in the water table, using wood dowels and rubber cord to simulate roots of very high or low stiffness, respectively. However, neither of these materials is a perfect analogue to the mechanical behaviour of real roots (see Liang *et al.* (2014)) and, to the best of the present authors' knowledge, testing under fully dynamic ground motions representative of real earthquake shaking has not previously been conducted. Again, this is in contrast to other potential methods of seismic slope reinforcement which have been investigated using dynamic centrifuge testing, including for geosynthetics (Nova-Roessig & Sitar, 2006) and piles (Al-Defae & Knappett, 2014).

The work presented herein will therefore investigate the dynamic behaviour of slopes reinforced with improved root analogues formed from acrylonitrile butadiene styrene (ABS) plastic using three-dimensional (3D) printing under a sequence of successive earthquake motions; analysis tools are also developed for linking the individual root–soil interactions to the global dynamic behaviour of the slope under a single motion or a series of successive motions. The root analogues will be shown to have mechanical properties

Manuscript received 13 October 2014; revised manuscript accepted 17 July 2015. Published online ahead of print 2 September 2015. Discussion on this paper closes on 1 May 2016, for further details see p. ii.

* University of Dundee, Dundee, UK.
† Technip, Aberdeen, UK (formerly University of Dundee, Dundee, UK).

more representative of real roots, and the use of successive motions might represent a sequence of strong motions occurring with insufficient intervening time for slope reinstatement. These tests will indicate the potential improvements to seismic performance of a slope which may be provided by the presence of vegetation.

The analytical modelling will consist of a two-stage process. First, a beam-on-non-linear-Winkler-foundation (BNWF) approach using existing p–y curves developed from piling engineering will be used to develop a computationally efficient macro-element for individual soil–root interaction that is analogous to pile response under lateral loading. The approach has been commonly used in analysing lateral soil–pile interaction, for example, by Boulanger *et al.* (2003), Allotey & Foschi (2005) and Knappett & Madabhushi (2009). The second stage is to add the force resistance contributions from roots of different diameters with different mechanical properties to produce a smeared zone of continuum material properties (e.g. additional representative cohesion) in place of the roots. The BNWF model is used to determine the soil–root interaction for different potential slip plane depths through the rooted soil, to define the variation of the smeared properties with depth. These smeared properties are finally used within a fully dynamic FE model in the time domain to simulate the global seismic response of the slope. This will build on procedures for the seismic response of fallow slopes presented by Al-Defae *et al.* (2013). The BNWF soil–root macro-elements are validated against a series of large direct shear tests with stress conditions mimicking those in the centrifuge models, and the whole procedure (macro-elements to smeared properties to dynamic FE modelling) will be validated against the centrifuge test data.

CENTRIFUGE MODELLING

Model preparation and soil properties

The centrifuge tests were performed using the Actidyn C67-2 geotechnical beam centrifuge located at the University of Dundee, UK, at a scale of 1:N where $N = 10$. The use of such a low scaling factor was felt to be the best compromise between the competing requirements of minimising grain size effects on the soil–root interaction (due to the generally small root analogue diameters, a lower value of N is desirable) and producing a prototype of the order of metres in height with as much low-frequency content as possible (both of these factors improve with a larger value of N). The earthquake simulator (EQS) used in this research is of a servo-hydraulic type, and is described in more detail in Liang (2015). Models were constructed within an equivalent shear beam (ESB) container, that is, one having flexible walls, with internal dimensions of 669 mm × 279 mm × 338 mm. Further information on the properties and performance of this specific container may be found in Bertalot (2013), while a wider discussion of the use of such containers for dynamic centrifuge modelling may be found in Zeng & Schofield (1996), Madabhushi & Teymur (2003) and Lee *et al.* (2013). All subsequent centrifuge properties and results are given at prototype scale except where otherwise indicated.

HST 95 Congleton silica sand was used in model construction, having the basic properties shown in Table 1 (after Lauder, 2010). For the centrifuge testing discussed herein, slopes were constructed by pluviation of dry sand through a predetermined height using a slot pluviator to level, followed by vacuum removal of excess sand to form the required slope. The slopes were constructed as a uniform deposit at a relative density of $I_D = 55$–60%, and had a height of 2·4 m from toe to crest, with a further 0·8 m of soil underneath. The slope angle was 27° (1:2), and it has been

Table 1. State-independent physical properties of HST 95 silica sand (after Lauder, 2010)

Property	Value
Specific gravity, G_s	2·63
D_{10}: mm	0·09
D_{30}: mm	0·12
D_{60}: mm	0·17
C_u	1·9
C_z	1·06
Maximum void ratio, e_{max}	0·769
Maximum void ratio, e_{min}	0·467

shown by Al-Defae *et al.* (2013) that a slope of similar angle was statically stable, yet with a low enough factor of safety (or yield acceleration) to maximise the magnitude of slip displacement during strong ground motion. The model configuration and instrumentation are shown in Fig. 1. In order to maximise the size of the slope, given the low scaling factor, the slope crest and toe were relatively close to the ESB container walls. However, this geometry was carefully chosen following initial limit analyses of the slope, which suggested that the seismic failure mechanism would lie within the geometry shown and would not be constrained by the boundaries. This will be confirmed later through the results of the FE simulations. ADXL78 micro-electromechanical system (MEMS) accelerometers manufactured by Analog Devices were embedded inside each model to measure the horizontal accelerations within the soil specimen, and three external linear variable differential transformers (LVDTs), with one installed at the centre of the crest and the other two placed adjacent to the side walls at different distances along the crest, were used to measure the settlement of the slope

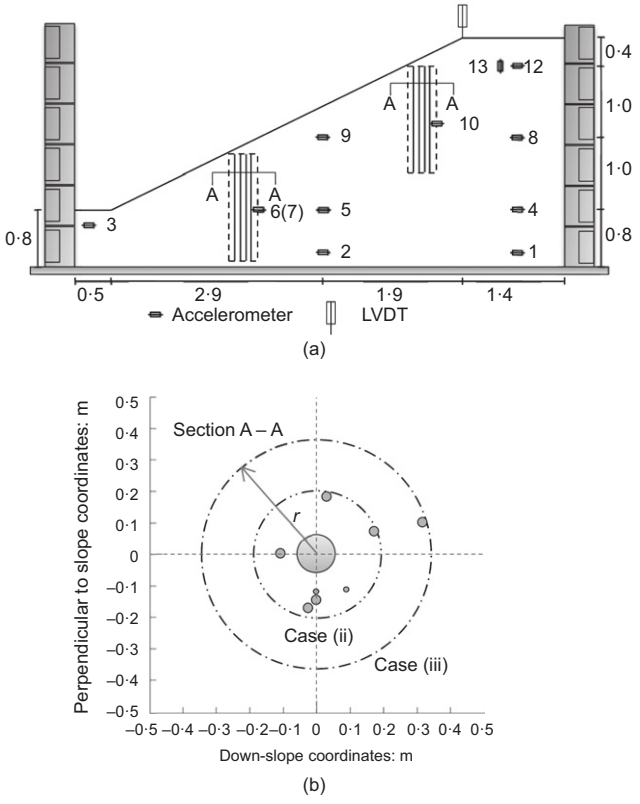

Fig. 1. Slope configuration: (a) centrifuge model layout and instrumentation (elevation); (b) distribution of root group (plan). All dimensions in m at prototype scale

crest and detect any boundary effects on this measurement. A circular disc with a diameter of 32 mm was placed between the surface of the slope and the tip of the LVDT to prevent the LVDT penetrating into the soil. The presence of such a disc may affect the ability of the LVDTs to record settlement at a single point. Further discussion of the disc effect will be discussed in the following section.

Two tests, referred to herein as TL03 and TL04, are presented here. The model slope TL03 was reinforced with straight root analogues with a predefined distribution (as shown in Fig. 1), and was designed to investigate the seismic performance of a reinforced vegetated slope under multiple successive earthquakes. The root analogues were 'printed' from ABS plastic, which has mechanical properties that are highly representative of plant root material. This study represents the first use of this material as a root analogue. Further details about the construction and material testing of these root analogues will be presented in the following section. The model TL04 was designed as a reference case for the model TL03, having identical slope geometry and soil properties, but fallow (no roots).

Eight successive earthquake motions were applied to each model at 10***g***, comprising three types with distinct peak ground acceleration (PGA), duration and frequency content. The first motion was taken from the 1995 Aegion earthquake (M_s 6·2) and was predicted to cause only a small amount of slip, predominantly acting to characterise the elastic dynamic behaviour of the slope. This initial motion was followed by three nominally identical stronger motions from the 1994 Northridge earthquake (M_s 6·8) and a further three from the 2009 L'Aquila earthquake (M_s 6·3), followed by a final Aegion motion to allow the changes in the elastic dynamic response to be determined following the sequence of larger motions. The three motions were downloaded from the Pacific Earthquake Engineering Research (PEER) NGA database and are presented in the time and frequency domains in Fig. 2 and Fig. 3, respectively. Each of the motions was band-pass filtered using a 512-point filter to obtain demand motions that were within the controllable range of the EQS. At 1:10 scale this range is between 4 Hz and 30 Hz (40–300 Hz at model scale). It should be noted that at 1:10 scale much of the low-frequency content of the original earthquake signal is lost; however, the compromise

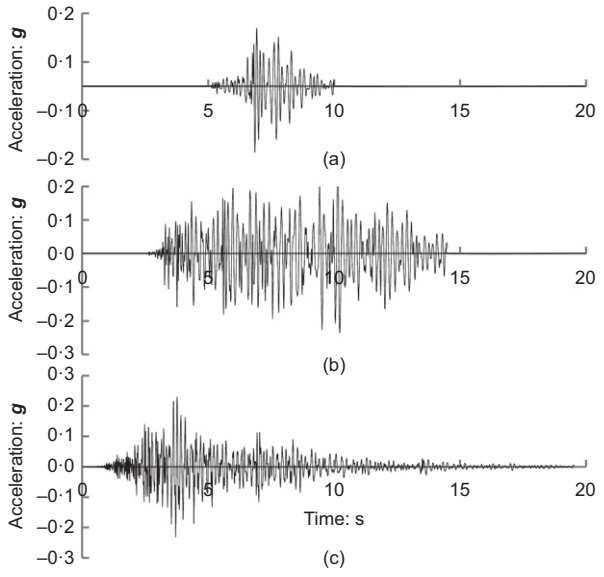

Fig. 2. Input bedrock motions in the time domain: (a) Aegion, 1995; (b) Northridge, 1994; (c) L'Aquila, 2009

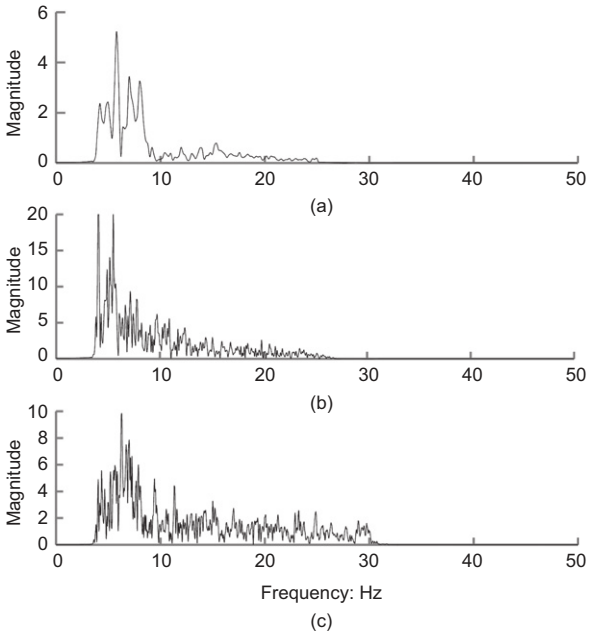

Fig. 3. Input bedrock motions in the frequency domain: (a) Aegion, 1995; (b) Northridge, 1994; (c) L'Aquila, 2009

of a low scale factor was necessary to minimise grain size effects between the root analogues and the soil grains, as mentioned previously. However, so long as the motions have large enough accelerations, it is still possible to exceed the yield acceleration of the slope cyclically and generate permanent slip. Once validated, FE models could later be used to investigate the effects of input frequency content on performance. The motions were calibrated on identical but un-instrumented 'dummy' slopes before formal testing to obtain motions which were as accurate and repeatable as possible. The sequence of motions is summarised in Table 2.

Model root characterisation

Liang *et al*. (2014) designed a simplified 3D root model cluster (length of 0·15 m at model scale) with root area ratio (RAR), root distribution and root length representative of 1:10 geometrically scaled tree root clusters for element and centrifuge testing. These complex 3D models are not discussed further in this paper, as to develop the analytical models it was decided to start with a simpler group of straight root analogues (but still having varying diameter and position). The straight analogues were selected to have the same RAR and spatial distribution at the level of the middle of the 3D root cluster; this is shown in Fig. 1(b). The middle cross-section was selected for two reasons: (*a*) RAR at the middle of the cluster was close to the mean RAR of the 3D cluster, which has in the past generally been considered as the

Table 2. Sequence of input motions

Motion ID	Input motion	Peak input acceleration: ***g***
EQ1	Aegion	0·12
EQ2	Northridge	0·28
EQ3	Northridge	0·28
EQ4	Northridge	0·28
EQ5	L'Aquila	0·23
EQ6	L'Aquila	0·23
EQ7	L'Aquila	0·23
EQ8	Aegion	0·12

major factor in root–soil interaction (e.g. Waldron, 1977; Pollen & Simon, 2005); and (*b*) the stump/main central tap root, which distinguishes tree root systems from herbaceous types, extended to 0·1 m depth from the ground surface at the model scale, and the effect of this could therefore be investigated. There were four 'blocks' of root analogues inserted within the centrifuge model slope: two near the crest of the slope and two towards the toe (the position of these two rows in elevation is shown in Fig. 1(a)).

The ABS plastic was selected as a material potentially having a very similar Young's modulus and ultimate tensile strength to real roots. Strength and stiffness were considered to be the most important characteristics in selecting an appropriate material. However, real roots have a cellular structure, with a number of overlying layers of tissue. Among them, the xylem and cambium layers play a significant role in mechanical behaviour, driving the characterisation of tensile strength and stiffness, respectively. The xylem tissue runs through the core of the root and consists of long, cylindrical cells that are joined from end to end and provide unidirectional fibre orientation (Karam, 2005). The cellular structure can be idealised as a stack of fibres aligned unidirectionally. To obtain a unidirectionally layered structure to the root analogues, they were fabricated using a Stratesys Inc. uPrint SE ABS rapid prototyper (also known as a 3D printer) at the University of Dundee, following the procedures outlined in Liang *et al.* (2014). The ABS plastic was delivered into the machine in the form of a spooled rod, which was melted and injected in successive layers onto a build platform by a moving print head. The whole printing procedure was controlled by a computer from a digital input file exported directly from the Solidworks 3D modelling software.

To characterise the mechanical properties of the layered root analogues, three-point bending flexural tests and uniaxial tensile testing of analogue specimens of various diameters were conducted, following the methods described in Liang *et al.* (2014); the results are shown in Fig. 4. The extreme fibre stress ρ_f plotted against flexural strain ε_f curves for the bending tests in Fig. 4(b) were derived from the applied load at midspan, F, and deflection at this point, Δ, using the following formulation

$$\sigma_f = \frac{8Fl}{\pi D^3} \quad (1)$$

$$\varepsilon_f = \frac{6\Delta D}{l_s^2} \quad (2)$$

where l_s is the root length and D is the root diameter. The value of σ_f at failure was defined as the modulus of rupture (MOR), while the tensile stress at failure in the uniaxial tension tests was defined as the ultimate tensile strength (UTS). In each case, failure was defined as the point at which the root analogues broke, indicated by the post-peak drop in stress in Fig. 4. These measures of strength are not necessarily the same due to the different modes of loading (bending and stretching, respectively). Fig. 5 shows that the new model root analogues perform as suitable substitutions of real roots – the 'real root' data in this figure are collated from the literature (Mickovski *et al.*, 2009; Warren *et al.*, 2009; Sonnenberg *et al.*, 2010; Mao *et al.*, 2012) from uniaxial tension tests on tree and shrub roots. It should be noted that bending test data were not available for the real roots in the database, and are not routinely collected for real plant roots. The stiffness of the root analogues is less representative than the strength, but is still a substantial improvement on previously used analogue materials such as rubber and wood, which are also shown in Fig. 5(b).

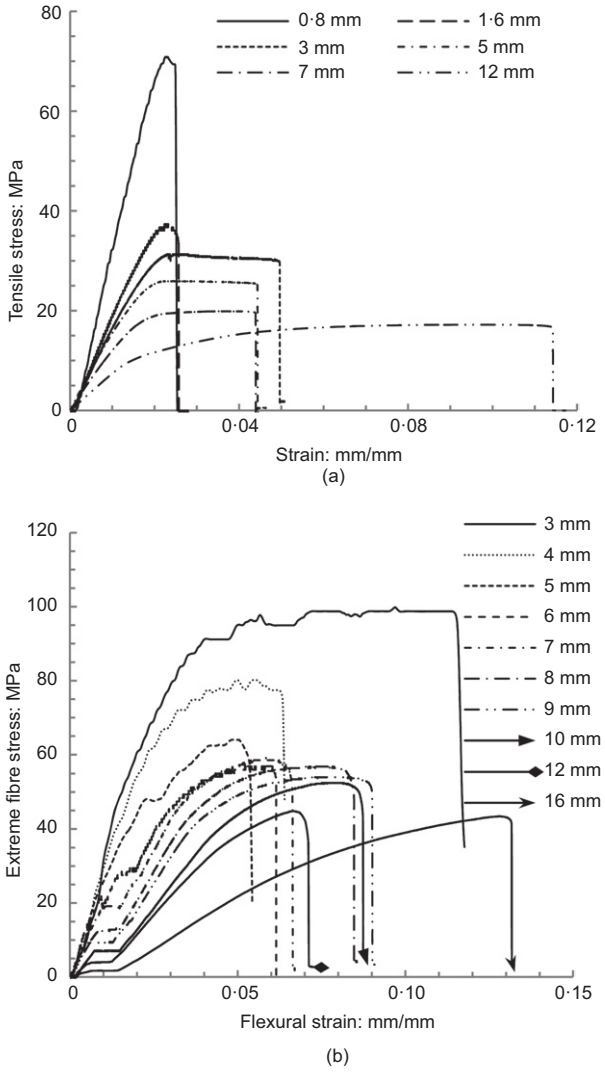

Fig. 4. Typical stress–strain curves for printed ABS plastic root analogues: (a) from uniaxial tensile testing; (b) from three-point flexural bending tests

Initial observations of seismic performance of rooted slopes

A comparison of the crest settlement between the root reinforced slope and unreinforced slope is shown in Fig. 6. Because of the potential effect of the settlement-reducing disc (as mentioned in the previous section), the settlement was confirmed by visual observations and measurements post-test. The presence of root analogues highly reduced the permanent slope settlement (61%) compared with the unreinforced cases, especially for the first two motions (EQ1 and EQ2). This can be interpreted as a result of the rapid mobilisation of root–soil interaction due to the initial soil slip under dynamic loading. Al-Defae & Knappett (2015) have demonstrated that, for the case of large vertical piles reinforcing slopes to significant depths, the full lateral restraint of the piles is mobilised within 2% of the pile diameter; applying this analogously to the root analogues here would suggest very rapid mobilisation due to the small root diameters. After the first two motions, relatively smaller reductions (in total 14%) were observed, which indicates that the additional resistive force of the root is largely constant after the initial rapid increase. The roots were not observed to have broken following careful post-test exhumation, which would infer that the maximum root–soil resistance was mobilised after EQ2 and that this was associated with yielding of the soil around the root analogues. For both

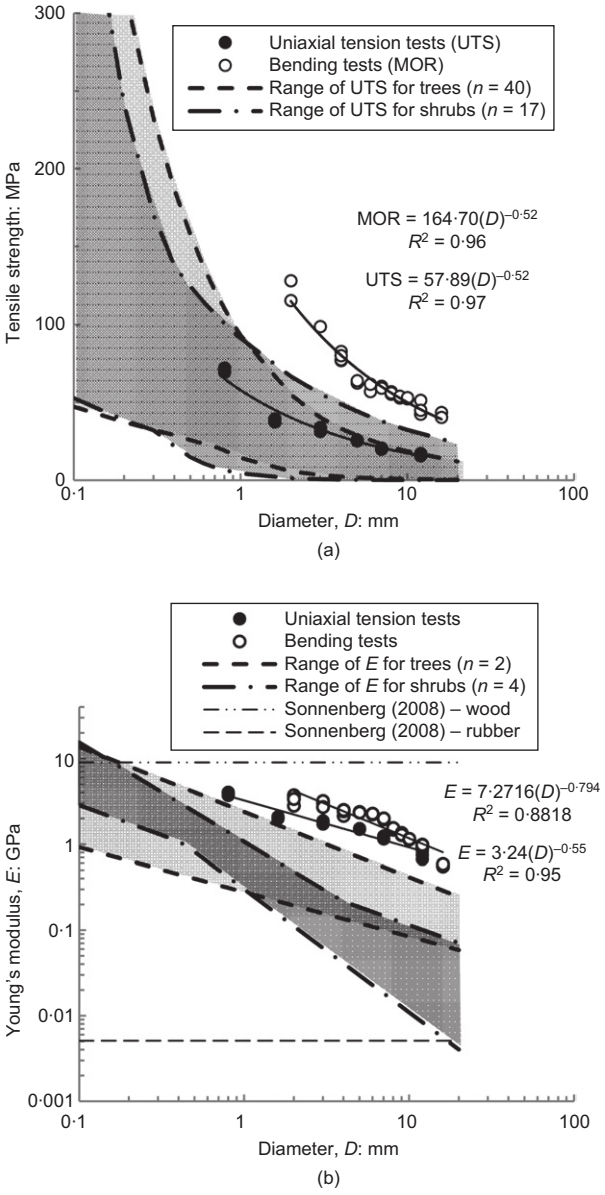

Fig. 5. Comparison of material properties between typical roots and root analogues: (a) tensile strength; (b)Young's modulus

root-reinforced and unreinforced slopes, a decreasing trend of settlement was observed when the slope was subjected to successive identical motions. This can be associated with the slope geometry change (re-grading), as previously proposed for fallow slopes by Al-Defae *et al.* (2013). Dynamic motions observed from the centrifuge tests will be discussed alongside results from numerical simulation later in the paper.

MODELLING ROOT–SOIL INTERACTION USING A BNWF APPROACH

The BNWF approach using existing *p–y* curves was conducted using the non-linear FE programme Abaqus as a convenient method to solve the beam-on-spring problem (although it should be noted that it would also be possible to complete the calculations using a finite-difference approach). A BNWF approach has significant advantages in computational efficiency compared to previous continuum FE models of root–soil interaction (e.g. Mickovski *et al.*, 2011), while offering significantly more detail in the response compared to simple models (e.g. Waldron, 1977; Pollen & Simon, 2005). Fig. 7 presents a schematic diagram of an individual soil–root system undergoing shear loading, as idealised within the BNWF approach. The root was modelled using deformable 'Timoshhenko' beam elements (which are flexible in both shear and bending) with constitutive behaviour defined by Timoshenko & Goodier (1970). A detailed description of the advantage of this element compared to simpler types may be found in Knappett & Madabhushi (2009). The root is discretised into elements non-uniformly along the length, with a higher concentration within the deformable zone ($0{\cdot}1l$ either side of the slip plane) after Randolph (1981). This was designed to provide additional computational efficiency. A linear elastic–perfectly plastic model was used to model the stress–strain behaviour of the root, which is a very reasonable approximation to the measured behaviour illustrated in Fig. 4. The Poisson ratio of ABS plastic was taken as 0·35. A series of dummy beams which sat at a uniform horizontal offset from the discrete nodes along the root were established to represent the free-field soil movement. A portion of horizontal rigid dummy beams on roller supports allowing horizontal movement (above the location of a potential shear plane) could move past the root without coming into contact. Non-linear *p–y* springs were then connected between roots and dummy beams. A full description of the *p–y* spring properties will be given in the following section. Soil deformation could be simulated by displacing the upper dummy beams laterally while fully restraining the lower beams. By re-meshing and changing the number of beams which were displaced, it was possible to simulate the soil–root interaction for any particular location of the slip plane passing through the rooted soil. A horizontal roller connection was attached at the tip of the root to prevent any unwanted vertical movement while allowing lateral displacement and rotation (as suggested by Duckett (2013)). Other than at this point, axial movement of the root was unrestrained.

p–y *modelling framework*

The non-linear *p–y* relationship derived by Reese *et al.* (1974) is employed in the modelling presented herein, which was derived from the results of full-scale pile testing in sands at Mustang Island. The use of this *p–y* modelling framework is beneficial given familiarity with the approach from piling engineering; however, there are a number of differences between root analogues and piles. First, plant roots are much smaller in diameter than piles (by approximately two orders of magnitude compared to the Mustang Island tests). Given that mobilised pile–soil resistance is expressed in terms of the diameter of the pile, and the lateral response (including the transition from rigid rotation to bending) is a function of slenderness (i.e. again expressed in terms of diameter), it follows that so long as continuum behaviour is still appropriate at small diameter, then the absolute size of the diameter should not have an effect. Second, owing to their increased flexibility, the lateral root analogue deformation will be much larger (5–42D) than traditionally occurs in laterally loaded piles. However, the *p–y* formulation includes a limiting capacity which is reached at low amounts of deformation, and so if there is no post-peak reduction in this capacity, then it is reasonable to assume that this capacity could be extended to larger deformations.

The Mustang Island tests were performed on steel piles for only one pile diameter and one type of sand. Owing to the limitation of the validation data, Brødbæk *et al.* (2009) discussed the practicability of this model and emphasised the effect of pile slenderness ratio on the initial stiffness of the *p–y* curve. The feasibility of this model for stiff piles with slenderness of $l/D < 10$ still requires investigation, as the

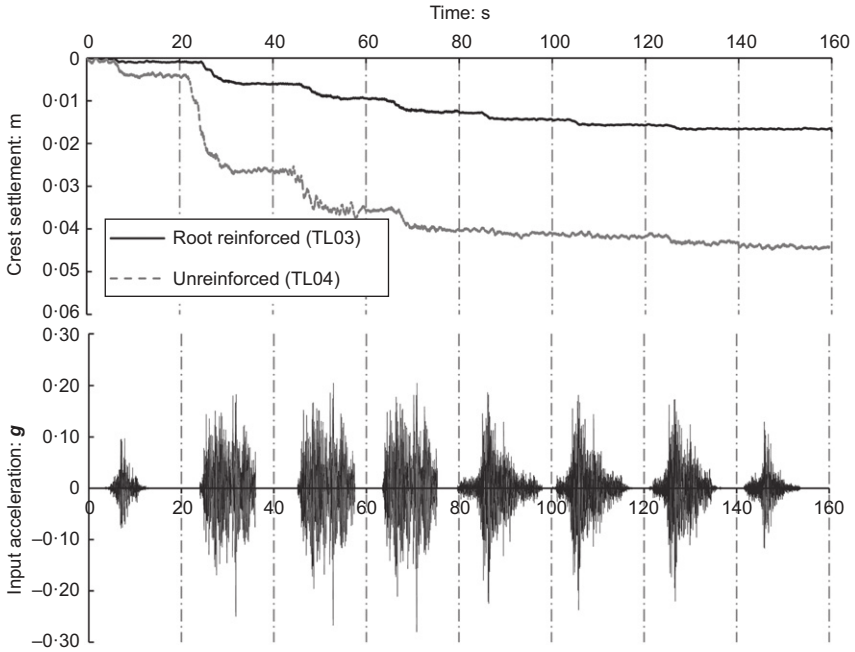

Fig. 6. Comparison of permanent crest settlement of fallow and rooted slopes from centrifuge testing

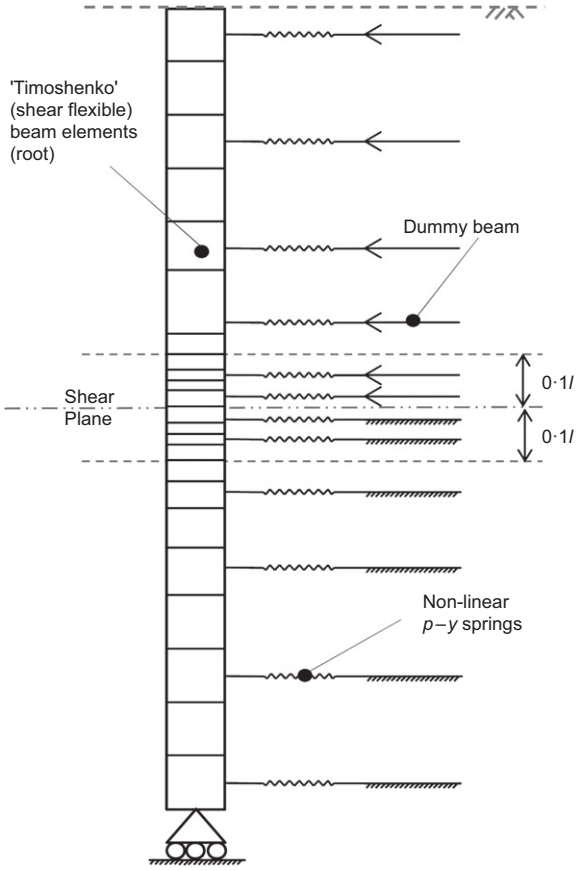

Fig. 7. Schematic diagram of root–soil system undergoing shear loading (BNWF model)

Mustang Island tests had a slenderness ratio of $l/D = 34{\cdot}4$. A summary of model root properties used in this project is given in Table 3, where the quantity column refers to an individual root block as shown in Fig. 1(a). This indicates that all of the root analogues had $l/D > 10$.

Table 3. Summary of root property (model scale)

Root ID	Diameter: mm	Length: mm	Slenderness: l/D	Quantity
1	12	150	12·5	1
2	3	150	50	6
3	1·6	150	93·75	2

As shown in Fig. 8, the p–y curves consist of four segments: an initial straight line p_1, a following parabolic section p_2, a connecting line p_3 and an upper border line p_4 characterised by the ultimate resistance, p_u. Two modes of failure were distinguished to define p_u, which depend on the pile embedded depth. At shallow depths, an unstable mass of soil is pushed upward along the connecting shear plane sitting in front of the pile to form a wedge, due to the low vertical confining stress in this zone. The ultimate resistance per unit length of pile for this mechanism can be calculated through equation (3). At greater depths, the sand flows around the pile as the additional vertical confinement suppresses the shallow mechanism, with the ultimate capacity of the soil against a flow mechanism being given

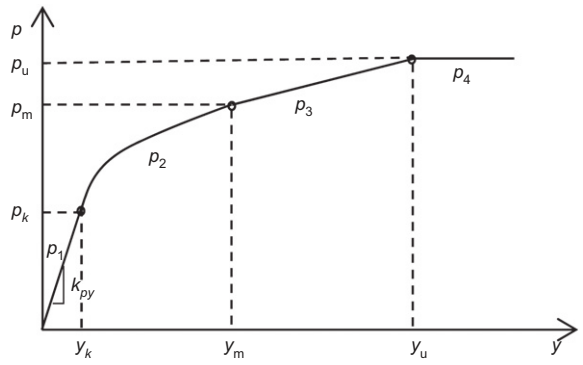

Fig. 8. p–y curve for piles in drained cohesionless soil (after Reese & Van Impe, 2011)

by equation (4).

$$p_{us} = \gamma' x \left[\frac{K_0 x \tan\phi \sin\beta}{\tan(\beta - \phi)\cos\alpha} + \frac{\tan\beta}{\tan(\beta - \phi)}(D + x \tan\beta \tan\alpha) + K_0 x \tan\beta(\tan\phi \sin\beta - \tan\alpha) - K_a D \right] \quad (3)$$

$$p_{ud} = K_a D \gamma' x(\tan^8\beta - 1) + K_0 D \gamma' x \tan\phi \tan^4\beta \quad (4)$$

In the foregoing equations, $\gamma' x$ represents the effective stress at any given depth, x. In the centrifuge tests, $\gamma' x$ is generated by the soil self-weight; to simulate the centrifuge stress conditions at the shear plane in the direct shear tests that are reported in the following section, the soil was subjected to an additional vertical surcharge load. In these cases, $\gamma' x$ was adjusted to be the actual normal effective stress in the direct shear test at the given depth. The angles α and β are used to define the geometry of the wedge, K_a and K_0 are the coefficients of active horizontal earth pressure and horizontal earth pressure at rest, respectively.

The initial straight line portion of the curve (p_1) was influenced by the initial subgrade reaction modulus k_{py}. Reese *et al*. (1974) suggest that the value of k_{py} only depends on the relative density of the sand, and for the dry soil density used in the centrifuge and subsequent shear box tests (see below) $k_{py} = 24{\cdot}4\ \mathrm{MN/m^3}$ was used in all BNWF simulations reported in the paper. The p–y curve described in this section represents the soil response per unit length of pile. To serve as the property of an individual spring in the BNWF approach, the values of p are scaled proportionally to the length of the element.

VALIDATION OF BNWF MODEL

Prediction of additional shearing resistance from root analogues

Laboratory shear tests were conducted to verify the BNWF model. As shown in Fig. 9, a large direct shear apparatus (DSA) with internal dimensions of 300 mm × 300 mm × 270 mm was purpose built for investigations into rooted soil. The shearing area is approximately the same as the model scale plan area of the sloping ground in the centrifuge. The DSA also allowed a shear displacement of 75 mm, much larger than a conventional DSA. This was necessary to ensure that soil containing ductile root analogues could be sufficiently deformed to mobilise the ultimate capacity of the reinforced soil. The same number and sizes of root analogues and density of soil as used in the centrifuge tests were used in the large DSA, although the model roots were here spaced at $s/D > 8$ to eliminate the group effect (Randolph, 2003). All measurements were corrected to remove the small force component due to friction between the two halves of the DSA frame, which was independently measured for tests with no soil. Fig. 10(a) shows the overall shearing resistance over the shear plane measured in the fallow and rooted tests and Fig. 10(b) shows a comparison between the inferred additional shear force provided by the roots from the DSA tests and as predicted by the BNWF simulations. The numerical value was found by integrating up the reaction forces of the p–y springs above the shear plane depth, while the experimental value was found as the difference in the shear box load measurement between the rooted and fallow cases (i.e. from Fig. 10(a)). The varied confining stress at the shear plane in the DSA was obtained by maintaining the same spatial distribution of root analogues and soil, and altering the surcharge weight to simulate homologous confining stress for different potential slip plane locations in the centrifuge test. It should be noted that DSA tests mentioned here could not be used directly to evaluate the realistic slip behaviour in a centrifuge test owing to the largely uniform confining stress along the length of the root analogues in the DSA (in the centrifuge this increases with depth from a value of zero at the ground surface).

The peak resistive forces in each case are summarised in Fig. 10(c). In Fig. 10 two cases are considered numerically: case I considers the use of root analogue material properties from three-point bending tests (i.e. Fig. 4(b)); case II, the use of material properties from uniaxial tensile tests (i.e. Fig. 4(a)). The comparison is necessary, as most existing analytical formulations of root contribution are based on the results of uniaxial tests which are much easier to conduct on real root specimens exhumed from the ground, particularly for very fine roots, see Wu (2013). Compared with an under-prediction in case II, a good match was observed in case I. This could be considered as evidence supporting the need to define root properties (at least for shear cases) through bending rather than uniaxial tests. At low effective stress (4 kPa), case II presents a slight under-prediction, suggesting that enhanced dilation should perhaps be considered at very low effective stress. Fig. 10(c) also demonstrates a positive correlation between the root resistive force and the vertical effective confining stress of the soil at the slip plane based on both numerical simulation and the laboratory shear tests. This is consistent with the behaviour of piles within a cohesionless soil and is supported by other recent work, for example, Duckett (2013). However the observations are inconsistent with current implementations of root reinforcement models in which typically a constant amount

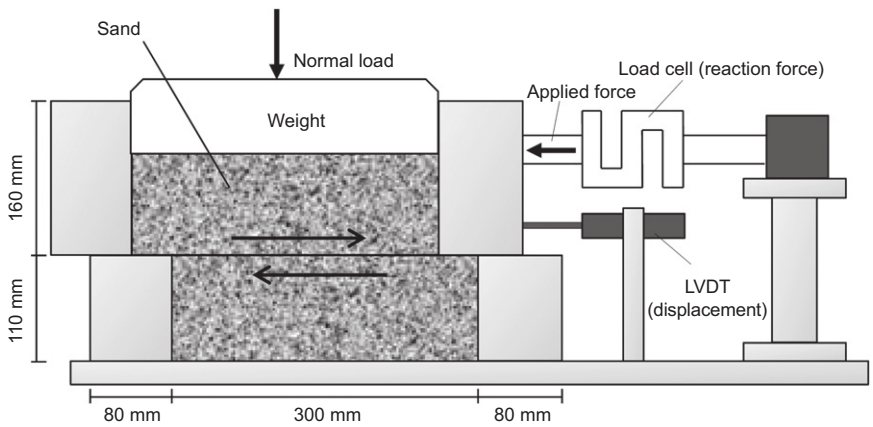

Fig. 9. Schematic diagram of large direct shear apparatus (DSA)

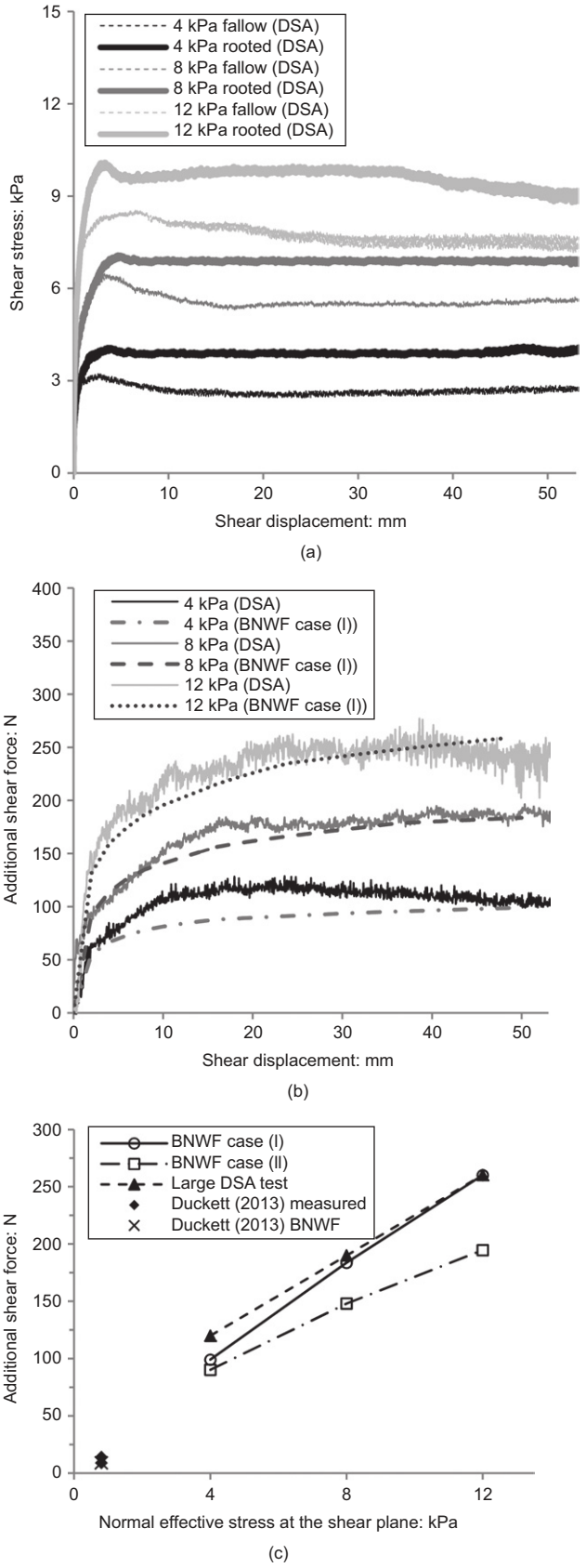

Fig. 10. (a) Measured shear resistances from DSA tests of fallow and rooted soil; (b) additional shearing resistance provided by root analogues, as measured in DSA and predicted using BNWF; (c) comparison of additional ultimate shear resistance from BNWF approach and laboratory DSA tests

of additional resistance with depth is used, as it is assumed that this is based only on the properties of the roots and is independent of the soil properties, which may vary with depth (Waldron, 1977; Pollen & Simon, 2005). The use of constant additional resistance with depth may be acceptable for grass root systems which penetrate only to very shallow depths, but for deeper rooting systems, the normal effective stress varies significantly due to the deeper embedding depth.

In each numerical case, critical state properties for the soil were considered (namely $\phi = 32°$). The reason for this was that the BNWF models are primarily used to obtain the representative additional shear strength of the roots (i.e. at large strain shear displacements of the rooted soil) for use in the later FE method (FEM) simulations (described below). Given that the diameter of the majority of the roots used is very small, it will only require relatively small global slip of the rooted soil to potentially induce large relative soil–root deformations. Therefore, by the displacement at which the rooted soil globally reaches critical state conditions most of the roots will have relative soil–pile shear strains much higher than this and will therefore be at p_u, as defined by the critical state of the local surrounding soil. Fig. 10(b) shows the additional combined resistive force from the root analogues, plotted against global shear displacement of the DSA for both the experiments and the BNWF simulations. Considering the 12 kPa case as an example, there is actually a series of small 'bumps' in the experimental data below 10 mm displacement which would be consistent with individual size classes of roots passing through peak behaviour at different global displacements (due to their different diameters). By the displacement at which the additional root contribution reaches its maximum level (beyond 20 mm or so, which is larger than the strain to critical state of ≈8% in fallow soil, after Al-Defae *et al.* (2013)) most, if not all, of the root–soil shearing will be at strains large enough for critical state locally, and this is why the BNWF simulations with critical state parameters generally fit well to the measured data at the larger displacements, which is where the additional root strength is defined.

Replication of failure mechanism

Soil–pile response depends on the flexibility of the pile (Brødbæk *et al.*, 2009). In terms of the root analogues, the behaviour of a rigid analogue and a flexible one subject to a soil movement of 0·05 m is compared in Fig. 11 These two analogues have identical root length ($l = 150$ mm) but different diameters ($D = 1{\cdot}6$ mm and 12 mm). For both analyses shown in Fig. 11, a significant difference in soil response was observed.

For the flexible analogue, the root deformation is governed by the soil movement; the upper part of the root moves similarly to the soil and the deformation zone is concentrated around the shear plane (between 0·05 m and 0·1 m depth). This causes stress concentration near the middle part of the root with it just reaching the yield point, as shown in Fig. 11(a). According to Fig. 11(b), the extreme fibre strain is approximately 0·046, which is just above the limiting material flexural strain inferred from the strength and stiffness relationships in Fig. 5 for 1·6 mm diameter ('elastic limit' strain at MOR) but above the strain at UTS (Fig. 4(a)). As the small analogues were not observed to snap, this suggests that there was some axial pull-through of the small roots at larger deformations which occurred at an axial force lower than that associated with the UTS. This is allowed for in the BNWF models as there is no restraint to axial movement at the top of the root (Fig. 7). Combining these observations, the flexible root would therefore be expected to show some

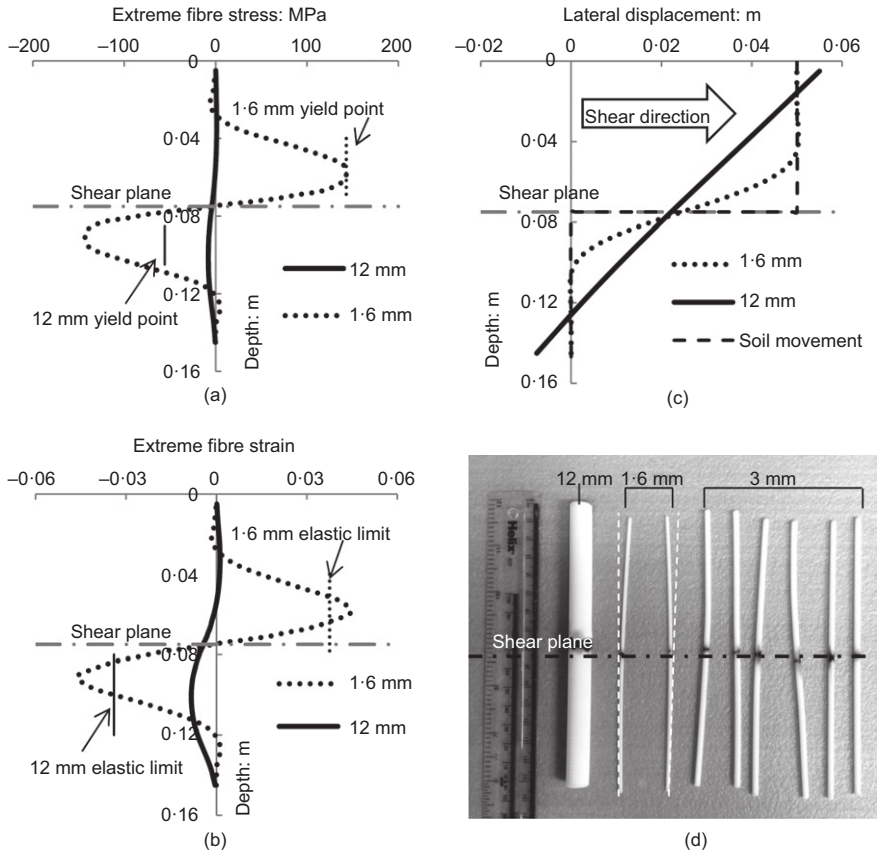

Fig. 11. Comparison of root analogue response under lateral loading for stiff and flexible roots: (a) extreme fibre stress (BNWF); (b) extreme fibre strain (BNWF); (c) lateral displacements (BNWF); (d) post-test observation of root analogues from laboratory DSA tests

irrecoverable bending deformation close to the shear plane when subjected to a soil movement of 0·05 m (which was exceeded within the laboratory DSA tests). Such behaviour corresponds well with the physical observations following the laboratory DSA test, as shown in Fig. 11(d). Conversely, the rigid root rotates significantly inside the soil with a translational slip of about 0·02 m and the performance is dominated by the root, which is shown to be well within the elastic range.

FINITE-ELEMENT MODELLING

The centrifuge tests were simulated numerically using Plaxis 2D in this study. Fifteen-noded triangular elements with 12 Gaussian points suitable for stress and collapse simulations were used. This element can simulate accurately the dynamic behaviour of slopes (e.g. Al-Defae *et al*., 2013). The mesh and boundary conditions are shown in Fig. 12. The boundary conditions, which allowed lateral deformation while reacting normal stresses and incorporated non-reflecting vertical boundaries, were established based on the theory proposed by Lysmer & Kuhlmeyer (1969) to simulate the semi-infinite soil condition. In this way, the performance of the boundary deformation in the ESB container can be controlled by the adjacent soil. This same procedure has previously been used by Al-Defae *et al*. (2013).

In each case, a dynamic ground displacement–time history was applied along the bottom of the slope. The input motions were obtained from the measurements at instrument 2 in the centrifuge tests, which represented the actual input motion the slope saw during the centrifuge tests. Before input, the measured motions were band-pass filtered to 4–30 Hz using an eighth-order Butterworth filter defined by a zero phase filtering method to eliminate any steady-state offset in the accelerometer recording.

The hardening soil model with small-strain stiffness (HS small, Schanz *et al*. (1999)) was used to model all soil units. This specific constitutive model has been verified to be effective at simulating the dynamic behaviour of HST 95 sand (Al-Defae *et al*., 2013). Model parameters used in the analyses are summarised in Table 4. All of the parameters apart from the cohesion c and damping ratio ζ_{add} (discussed later) could be collected from the aforementioned literature. The performance of this model at estimating the shear modulus and damping within the centrifuge tests is described later.

Root–soil matrix modelling

To model the dynamic behaviour of a slope with regions of different strength in FE analysis, it is feasible to consider the slope as a composite set of different soil blocks (Figs 12(a) and 12(b)), with the soil–root interaction behaviour from the BNWF approach mentioned previously being used to quantify the additional strength and stiffness in the rooted zones.

The strength of root reinforced soil is typically evaluated from the following equation based on the Mohr–Coulomb failure criterion after Waldron (1977)

$$\tau = \sigma' \tan \phi' + c' + c'_r \quad (5)$$

where c'_r represents the additional shear strength contribution due to the presence of roots, with ϕ' and c' representing the strength properties of the fallow soil. Given that the additional resistance from the roots was found to increase with the depth of the shear plane (Fig. 10(c)), this was incorporated through increasing the c' value in the rooted zones above that for the soil alone (i.e. zero) and this parameter was varied with depth to simulate the depth effect

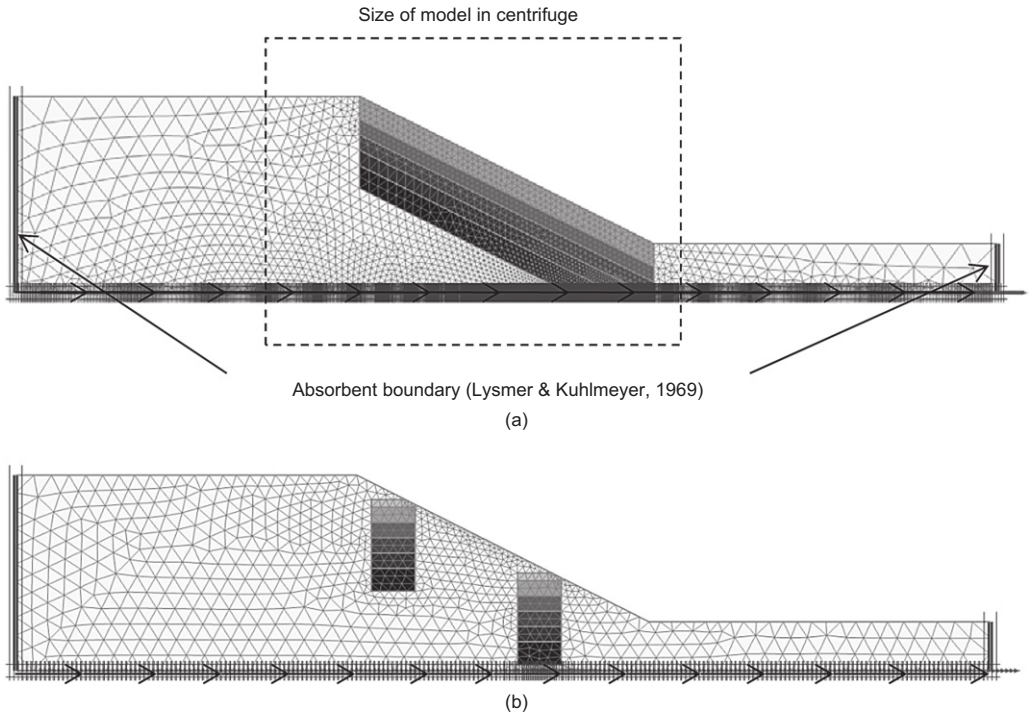

Fig. 12. Finite-element mesh, showing boundary conditions: (a) case (i); (b) cases (ii) and (iii)

Table 4. Key parameters and properties of HST 95 silica sand for HS small strain model (after Al-Defae *et al.*, 2013)

Parameter	Value
ϕ'_{pk}: degrees	32
ψ': degrees	0
γ_{unsat}: kN/m^3	16·0
γ_{sat}: kN/m^3	16·0
E_{50}^{ref}: MPa	42·5
E_{oed}^{ref}: MPa	34
E_{ur}^{ref}: MPa	102
ν_{ur}	0·2
G_0^{ref}: MPa	116·3
m'	0·55
$\varepsilon_{s,0\cdot7}$: %	0·016
R_f	0·9

as shown in Fig. 10. This is indicated in Fig. 12 by the variation in shading with depth within the rooted zones.

To determine the appropriate value of c'_r and its variation with position in the plane of failure within the continuum FE model the rooted soil zones were represented by a plane cross-section taken horizontally through model roots as illustrated in Fig. 1(b). At a sufficient distance, r, away from the centre of the main taproot, the effect of the root reinforcement may be expected to have reduced to a negligible amount. Limited literature (Yegian & Wright, 1973) is available on the determination of the zone of the root group influence, especially for the case herein, which has variable diameter distribution. Herein, three cases are considered to investigate the influence zone of the roots: in case (i) the reinforcement effect is uniformly distributed along the whole slope face; in case (ii) the influence radius r is selected based on the actual extreme boundary of the root analogues; and in case (iii) r is equal to three times the diameter of the trunk, as shown in Fig. 1(b). Cases (i) and (ii) represent two extreme cases, while case (iii) was established considering the group efficiency at $3D$ spacing to be 0·6–0·8 for the main row in medium dense sand based on a body of literature (e.g. McVay *et al.*, 1995, 1998; Rollins *et al.*, 2005). The two-dimensional (2D) plane strain FE model assumes that stress distribution in every longitudinal section along the length, b, of the 3D slope geometry is equal (i.e. in the out-of-plane direction). For the rooted case considered here, two root groups were placed along the length of the 3D slope in the centrifuge, so that the equivalent (smeared) area, A, of shear plane per metre length of the slope over which the additional root strength acts is given by

$$A = r\frac{b}{2} \tag{6}$$

Having evaluated the value of A for the rooted zone for each of the three cases (i)–(iii), BNWF simulations were run for each of the different root diameters separately considering the shear plane at different depths, with the p–y spring properties evaluated for the prototype effective stress conditions in the centrifuge tests (rather than the 'model scale with surcharge' simulations for the laboratory DSA tests). This is shown in Fig. 13(a). However, in the centrifuge, the model root groups were installed into the slope vertically, rather than perpendicular to the soil surface (as in the DSA). Modifications of the p–y curve due to the sloping ground effect were therefore made, after Reese & Van Impe (2011). The wedge-type failure mechanism only was modified as the flow-around failure has not been previously observed to be influenced by sloping ground (Reese & Van Impe, 2011). The ultimate soil resistance in this mode is therefore given by

$$\begin{aligned} p_{us} = \gamma' x \Bigg[& \frac{K_0 x \tan\phi \sin\beta}{\tan(\beta-\phi)\cos\alpha}(4t_1^3 - 3t_1^2 + 1) \\ & + \frac{\tan\beta}{\tan(\beta-\phi)}(Dt_2 + xt_2^2 \tan\beta \tan\alpha) \\ & + K_0 x \tan\beta(\tan\phi \sin\beta - \tan\alpha)(4t_1^3 - 3t_1^2 + 1) \\ & - K'_a D \Bigg] \end{aligned} \tag{7}$$

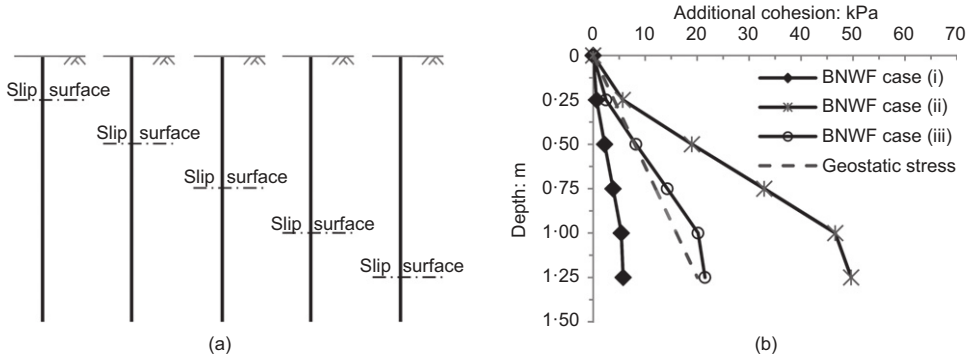

Fig. 13. Apparent root cohesion for the three cases: (a) assumed slip surface; (b) variation of root cohesion with depth as predicted from BNWF

$$t_1 = \frac{\tan\beta \tan\theta}{1 - \tan\beta \tan\theta} \tag{8}$$

$$t_2 = 1 + t_1 \tag{9}$$

$$K'_a = \cos\theta \frac{\cos\theta - \sqrt{\cos^2\theta - \cos^2\phi}}{\cos\theta + \sqrt{\cos^2\theta - \cos^2\phi}} \tag{10}$$

For each shear plane depth, the additional resistive force provided by each root was added together using

$$F_p = k \sum_{n=1}^{n} (F_r^n \cdot N_n) \tag{11}$$

where n is the number of distinct types/geometries of model root, reflecting the diversity of the root diameter and N is the quantity of the model roots of a given type (see Table 3). For the particular distribution of roots used in the centrifuge tests, a group-effect reduction factor was required to model root–soil–root interaction; this parameter is represented by k in equation (11). Further DSA tests, which were arranged in exactly the same way as the centrifuge tests, were performed. Through comparing the additional resistive force in these tests with the 'widely spaced roots' case reported previously, a value of $k = 0{\cdot}78$ was found. This value was then applied to the BNWF analyses for the centrifuge simulations.

The apparent root cohesion c'_r was determined in each of cases (i)–(iii) as the additional resistive force per area of specific shear plane at each depth, that is

$$c'_r = F_p / A \tag{12}$$

The resulting variations of c'_r with depth for cases (i)–(iii) are illustrated in Fig. 13(b).

The DSA test indicated a negligible change of shear stiffness of rooted soil at the largest confining stress of 12 kPa on the slip plane (these data are shown in Fig. 14(a)). A similar phenomenon was observed for testing at other confining stresses (not shown). Measurements made from the buried accelerometers in the centrifuge tests indicated a similar result; here the data points were determined from second-order estimates, following the method outlined by Brennan *et al.* (2005). It can also be found from Fig. 14 that the damping ratios for both fallow and rooted models lay along a similar trend. As a result it was assumed in the FE analysis that the effect of the roots could be incorporated as an additional cohesion only, added to the underlying properties of the HST 95 sand. A good match was subsequently observed between centrifuge measurement and numerical simulation on shear stiffness (see Fig. 14(a)); the data points for the numerical simulations were

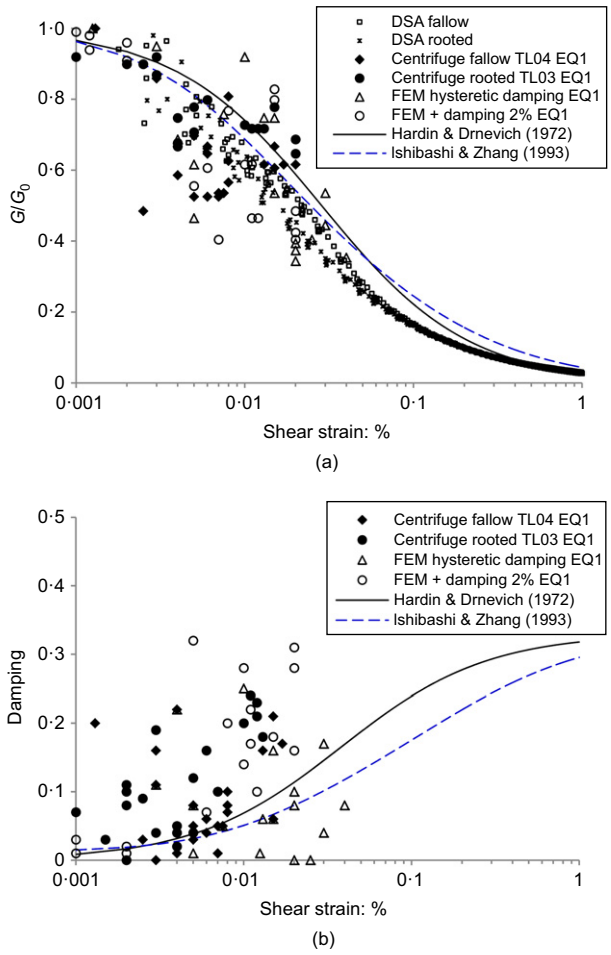

Fig. 14. (a) Shear modulus degradation and (b) damping as measured in centrifuge tests, DSA tests and FEM simulations of fallow and rooted slopes, and comparison to previously published curves

determined in the same way as in the centrifuge tests, using data from 'virtual' accelerometers at homologous points within the FE mesh. Material hysteretic damping within the numerical model was generally smaller than that inferred from the centrifuge tests (see Fig. 14(b)). This indicates that a small amount of additional damping was required for the soil model to accurately simulate the seismic behaviour of HST 95 sand as observed in the centrifuge tests. Further details about the determination of such additional damping will be given later. Fig. 14 also shows some models from the literature (Hardin & Drnevich, 1972; Ishibashi & Zhang, 1993) for comparison.

VALIDATION OF FEM

The key indicators of slope performance considered herein are: (*a*) peak ground accelerations at the slope crest; and (*b*) crest settlement.

Fallow slope

Figure 15 shows a comparison of measured and simulated accelerations and settlement at the crest of the slope in the earthquake sequence of TL04. The HS small model has inherent hysteretic damping when subjected to cyclic loading (Brinkgreve *et al.*, 2007). But according to Fig. 15(a), significant over-prediction of accelerations was observed. This appears to be associated with the increased amplification of lower frequency (<4 Hz) and higher frequency (>15 Hz) components, as shown in Fig. 15(b). Al-Defae *et al.* (2013) reported that additional Rayleigh damping was required to supplement the inherent hysteretic material damping to match ground accelerations when validating a similar FE model against centrifuge tests of a larger slope at 1:50 scale. Rayleigh damping was therefore added to the HS small model, where the equivalent additional viscous damping is given by

$$\zeta_{\text{add}} = c_{\text{m}}\left(\frac{1}{4\pi f_{\text{n}}}\right) + c_k(\pi f_{\text{n}}) \tag{13}$$

Additional damping of approximately 2% at the frequencies of 4 and 30 Hz was determined after several attempts, resulting in values of $c_{\text{m}} = 0{\cdot}8870$ and $c_k = 0{\cdot}0001872$. Al-Defae *et al.* (2013) proposed different parameters corresponding to 5% additional viscous damping and proposed that this was required as a result of imperfect replication of the semi-infinite boundary condition by the ESB box in the centrifuge. This would be consistent with a different required damping in this study as the stiffness of the rubber inter-layers in the ESB is normal-stress dependent and so will vary with ***g***-level (Bertalot, 2013), and so the container will necessarily perform differently at different values of *N*. Both the crest accelerations and permanent settlement with the additional damping simultaneously gave a good match between the FE simulation and the centrifuge test.

Figure 16 shows the accumulated shear strain at the end of the eight earthquakes from the fallow FE model. This indicates that the failure mechanism intersected the slope crest within the boundaries of the ESB container and that it also passed through the toe of the slope, therefore avoiding any potential restraint to motion of the container wall on both sides. This supports the initial decisions regarding optimising the geometry of the slope within the constraints provided by the low scaling factor.

Rooted slope

The simulated accelerations for the three cases at the crest of the slope (instrument 12), compared with those measured from TL03, are shown in Figs 17(a) and 17(b), in both time and frequency domains, respectively. The accelerations without any additional damping in the three cases for root modelling are shown in terms of the envelope of peak values and generally demonstrate significant over-prediction. It seems that there are some effects of the variation of soil cohesion spatial distribution on the ground motion

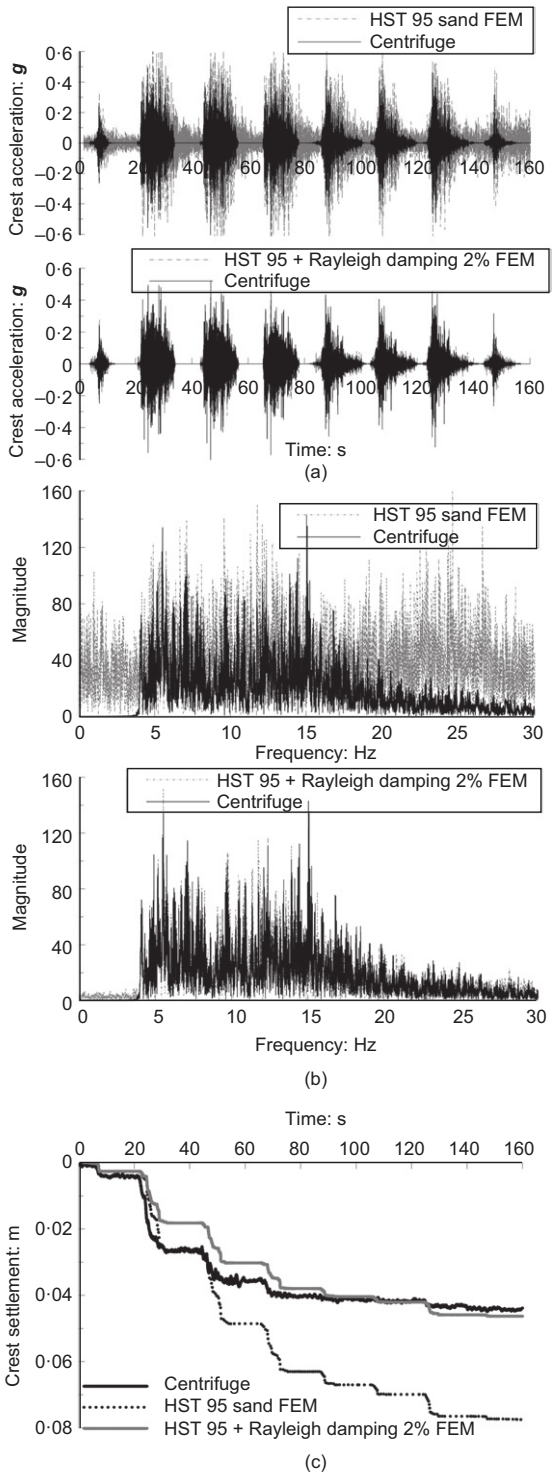

Fig. 15. Comparison of measured and predicted acceleration and permanent settlement at crest of fallow slope during test TL04: (a) accelerations in time domain; (b) accelerations in frequency domain; (c) settlement

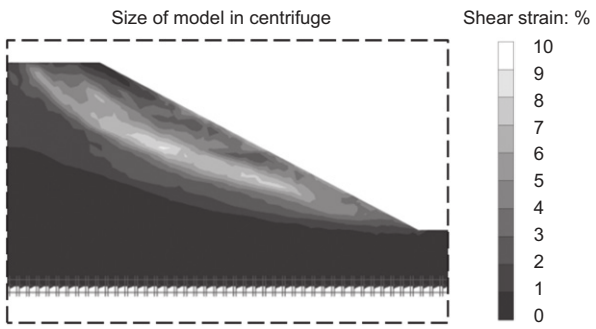

Fig. 16. Shear strain distribution within fallow FE model (end of simulation)

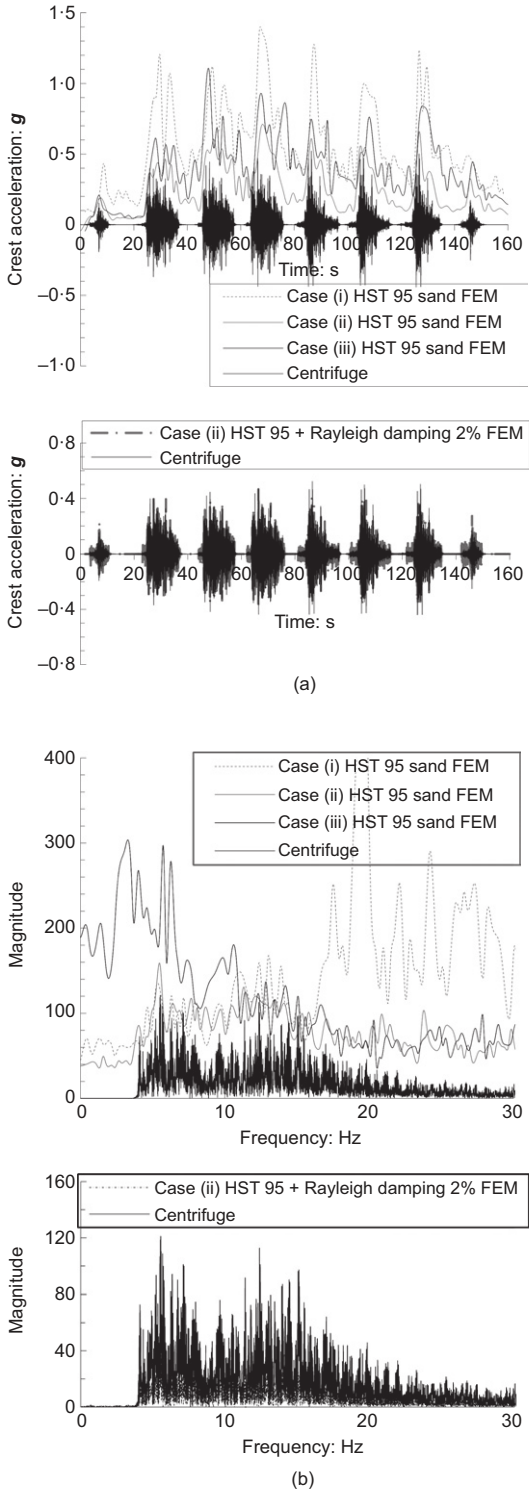

Fig. 17. Comparison of measured and predicted acceleration at crest of rooted slope for three root modelling cases during test TL03: (a) time domain; (b) frequency domain

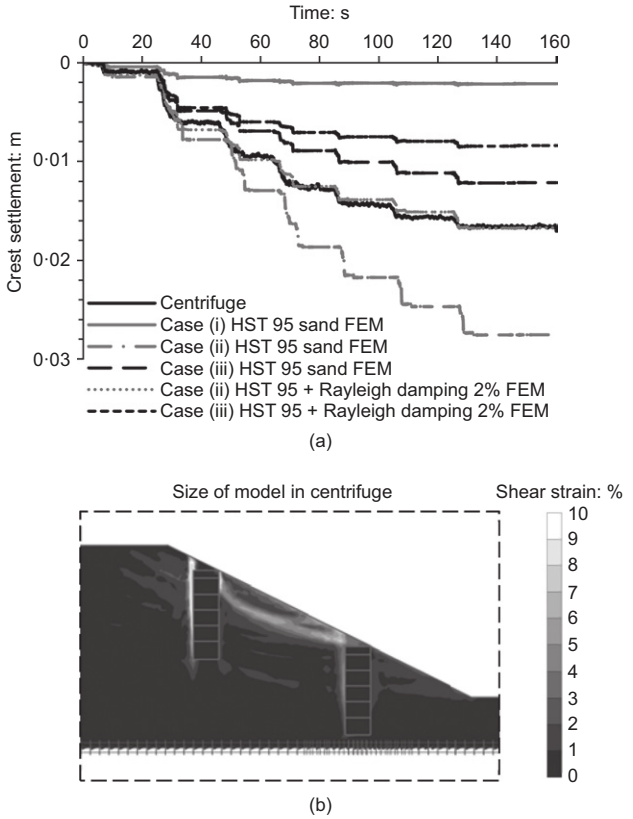

Fig. 18. (a) Comparison of measured and predicted permanent crest settlement for three cases of root modelling during test TL03; (b) shear strain distribution within rooted FE model (end of simulation, case ii)

propagation, as significant differences were observed between the three cases. When Rayleigh damping was added to the model, a good match was observed for all three cases, but case (ii) with damping ratio of 2% appeared to give the best match. This damping ratio corresponds to that in the unreinforced slope, and suggests that the root analogues do not add additional damping to the soil. Case (ii) is illustrated in the figure to show the agreements.

Figure 18(a) presents a comparison of the permanent crest settlement for the three root modelling cases against the centrifuge test measurements. In contrast with cases (i) and (iii), case (ii) successfully captures the pattern of settlement, specifically the root strength mobilisation in the first two motions and the re-grading effect in the subsequent motions, and this case also shows the best match simultaneously to the crest acceleration (Fig. 17). This suggests that the root–soil interaction obtained from the BNWF macro-element modelling is consistent with the global dynamic behaviour of the rooted slope. It also suggests that it is important in modelling the boundary value problem not to distribute additional resistance uniformly across the slope (as in case (i)), but to know the boundaries of the zone where the roots are. Fig. 18(b) shows the accumulated shear strain in case (ii) for comparison with the fallow case (Fig. 16). It can again be seen that the failure mechanism is well fitted to the size of the centrifuge model and also, interestingly, the figure shows how the rooted zones act to buttress the slope, almost acting like soft retaining walls. This fundamental change in mechanism may explain why the crest settlement is so sensitive to the spatial distribution of the root reinforcement (i.e. case (i), (ii) or (iii)).

CONCLUSIONS

Dynamic centrifuge testing has been performed to investigate the performance of slopes containing root analogues under a sequence of earthquake motions. Three-dimensional printing of layered ABS plastic was used to produce repeatable root analogues which are highly representative of the mechanical behaviour of real roots. The observed slope behaviour has been simulated using a two-stage approach in which a BNWF approach using existing p–y curves was employed to evaluate individual

root–soil interaction, and this information was then used to evaluate equivalent smeared properties for use in plane strain continuum FE analysis. The whole numerical simulation approach was validated against the centrifuge test data. The following principal conclusions can be drawn from the study:

(*a*) Reduction of up to 61% in permanent crest settlement was observed for the small height prototype slope (1:2 slope, height 2·4 m) considered herein which was 'planted' with root analogues. The reduction mainly occurs in the first two motions (which cause the largest amounts of slip) due to the mobilisation of the root–soil interaction.

(*b*) The BNWF macro element approach gave comparable prediction of the performance of the particular soil–root analogue system considered when undergoing monotonic shear loading. The root behaviour appeared to be dominated by transverse bending rather than axial tension when subjected to lateral soil movement. This suggests that the measurement of root material properties for slope stability analyses should therefore take into account this mode of deformation, and root–soil interaction models based on axial response may not correctly estimate the available mechanical soil reinforcement from roots.

(*c*) Continuum FE analysis using appropriately sized zones of smeared rooted soil properties derived from the BNWF macro elements was validated to be effective at simulating the global dynamic performance of the slope reinforced with root analogues that was considered in the study. The influence zone of root groups is complex, but when simplified to the boundary geometry that the root group actually occupies, it appears to provide a very reasonable simulation.

(*d*) Consistency was observed between dynamic acceleration and permanent soil movements in the FE simulations. A small amount of additional viscous damping was required to achieve the best match to the centrifuge data.

(*e*) The root analogues tested provided additional shear strength to the soil, but did not have an appreciable effect on modifying the soil stiffness or damping.

It should be noted that further centrifuge testing and accompanying DSA testing with different root properties/distributions, soil properties and slope geometries would be required to generalise these conclusions.

ACKNOWLEDGEMENTS

The authors would like to express their sincere gratitude to Mark Truswell, Colin Stark and Gary Callon at the University of Dundee for their assistance in printing the model root analogues and undertaking the centrifuge test programme. The first author would like to acknowledge the financial support of the China Scholarship Council.

NOTATION

A area of plane
b width of slope
C cohesion of soil
C coefficient related to stress level
C_u coefficient of uniformity
C_z coefficient of curvature
c_k stiffness proportional, Rayleigh damping coefficient
c_m mass proportional, Rayleigh damping coefficient
c' cohesion of the soil
c'_r additional cohesion due to the presence of root
D diameter of pile or root
D_{10} particle diameter at which 10% is smaller
D_{30} particle diameter at which 30% is smaller
D_{60} particle diameter at which 60% is smaller
E Young's modulus
E_{50}^{ref} triaxial secant stiffness (at 50% of deviatoric failure stress in drained triaxial compression)
E_{oed}^{ref} oedometric tangent stiffness (in compression)
E_{ur}^{ref} unloading–reloading stiffness
e_{max} maximum void ratio
e_{min} minimum void ratio
F force
F_p force resistance for a pile or root group
F_r force resistance for a single root
f_n natural frequency
G_s specific gravity
G_0^{ref} small strain modulus
g acceleration due to gravity($= 9{\cdot}81$ m/s^2)
I_D relative density
K_a coefficient of active earth pressure at rest
K'_a coefficient of active earth pressure at rest for sloping ground
K_0 coefficient of earth pressure at rest
k coefficient for group efficiency
k_{py} initial modulus of subgrade reaction
l length of pile
l_s span of root in material testing
m slope of p–y curve
m' power-law index for stress-level
N code of model root
n quantity
p reaction from soil due to deflection of pile
p_k specific soil reaction on p–y curves for sand
p_m specific soil reaction on p–y curves for sand
p_u specific soil reaction on p–y curves for sand
r radius of soil and root matrix
R_f ratio of deviatoric failure stress to asymptotic limiting deviator stress
t vertical shear force between inclusion and soil
x depth of the soil
y lateral deflection
y_k specific deflection on p–y curves for sand
y_m specific deflection on p–y curves for sand
y_u specific deflection on p–y curves for sand
α angle to define geometry
β angle to define geometry
Δ transverse deflection in bending test
γ_{unsat} unsaturated unit weight
γ_{sat} saturated unit weight
γ' effective unit weight
ε_f flexure strain
$\varepsilon_{s,0{\cdot}7}$ shear strain at $G/G_0 = 0{\cdot}7$
ζ_{add} additional Rayleigh damping ratio
θ slope angle
ν Poisson ratio
ν_{ur} Poisson ratio (unload–reload)
σ normal effective stress
σ_f flexure stress
τ shear stress
ϕ' effective angle of friction
ϕ'_{pk} (secant) peak angle of friction
ψ' effective angle of dilation

REFERENCES

Al-Defae, A. H. & Knappett, J. A. (2014). Centrifuge modeling of the seismic performance of pile-reinforced slopes. *J. Geotech. Geoenviron. Engng* **140**, No. 6, 1–13.

Al-Defae, A. H. & Knappett, J. A. (2015). Newmark sliding block model for pile-reinforced slopes under earthquake loading. *Soil Dynam. Earthquake Engng* **75**, 265–278.

Al-Defae, A. H., Caucis, K. & Knappett, J. A. (2013). Aftershocks and the whole-life seismic performance of granular slopes. *Géotechnique* **63**, No. 14, 1230–1244, http://dx.doi.org/10.1680/geot.12.P.149.

Allotey, N. & Foschi, R. (2005). Coupled p–y t–z analysis of single piles in cohesionless soil under vertical and/or horizontal ground motion. *J. Earthquake Engng* **9**, No. 6, 755–775.

Ausilio, E., Conte, E. & Dente, G. (2000). Seismic stability analysis of reinforced slopes. *Soil Dynam. Earthquake Engng* **19**, No. 3, 159–172.

Bertalot, D. (2013). *Foundations on layered liquefiable soils*. PhD thesis, University of Dundee, Dundee, UK.

Boulanger, R., Kutter, B. & Brandenberg, S. (2003). *Pile foundations in liquefied and laterally spreading ground during earthquakes: centrifuge experiments and analyses*, Report no. UCD/CGM-03/01. Davis, CA, USA: University of California.

Brennan, A., Thusyanthan, N. I. & Madabhushi, S. P. G. (2005). Evaluation of shear modulus and damping in dynamic centrifuge tests. *J. Geotech. Geoenviron. Engng* **131**, No. 12, 1488–1497.

Brinkgreve, R., Kappert, M. & Bonnier, P. (2007). Hysteretic damping in a small-strain stiffness model. In *Numerical models in geomechanics, Proceedings of NUMOG X*, Rhodes, Greece (eds S. Pietruszczak and G. N. Pande), pp. 737–742. London, UK: Taylor & Francis Group.

Brødbæk, K. T., Møller, M., Sørensen, S. P. H. & Augustesen, A. H. (2009). *Review of p–y relationships in cohesionless soil*, DCE Technical Report no. 57. Aalborg, Denmark: Aalborg University.

Duckett, N. (2013). *Development of improved predictive tools for mechanical soil–root interaction*. PhD thesis, University of Dundee, Dundee, UK.

Hardin, B. O. & Drnevich, V. P. (1972). Shear modulus and damping in soils: design equations and curves. *Soil Mech. Found. Div.* **98**, No. SM7, 667–692.

Ishibashi, I. & Zhang, X. (1993). Unified dynamic shear moduli and damping patios of sand and clay. *Soils Found.* **33**, No. 1, 182–191.

Karam, G. N. (2005). Biomechanical model of the xylem vessels in vascular plants. *Ann. Botany* **95**, No. 7, 1179–1186.

Knappett, J. A. & Madabhushi, S. P. G. (2009). Influence of axial load on lateral pile response in liquefiable soils. Part II: numerical modelling. *Géotechnique* **59**, No. 7, 583–592, http://dx.doi.org/10.1680/geot.8.010.3750.

Kourkoulis, R., Gelagoti, F., Anastasopoulos, I. & Gazetas, G. (2011). Slope stabilizing piles and pile-groups: parametric study and design insights. *J. Geotech. Geoenviron. Engng* **137**, No. 7, 663–677.

Lauder, K. (2010). *The performance of pipeline ploughs*. PhD thesis, University of Dundee, Dundee, UK.

Lee, S. H., Choo, Y. W. & Kim, D. S. (2013). Performance of an equivalent shear beam (ESB) model container for dynamic geotechnical centrifuge tests. *Soil Dynam. Earthquake Engng* **44**, 102–114.

Liang, T. (2015). *Seismic performance of vegetated slopes*. PhD thesis, University of Dundee, Dundee, UK.

Liang, T., Knappett, J. A. & Bengough, A. G. (2014). Scale modelling of plant root systems using 3-D printing. In *Physical modelling in geotechnics – Proceedings of the 8th international conference on physical modelling in geotechnics 2014, ICPMG 2014*, Perth, Australia (eds C. Gaudin and D. White), vol. 1, pp. 361–366. CRC Press, Taylor & Francis Group.

Lin, D. G., Huang, B. S. & Lin, S. H. (2010). 3-D numerical investigations into the shear strength of the soil–root system of Makino bamboo and its effect on slope stability. *Ecol. Engng* **36**, No. 8, 992–1006.

Lysmer, J. & Kuhlmeyer, R. L. (1969). Finite dynamic model for infinite media. *J. Engng Mech.* **95**, No. 4, 859–875.

Madabhushi, S. P. G. & Teymur, B. (2003). Experimental study of boundary effects in dynamic centrifuge modelling. *Géotechnique* **53**, No. 7, 655–663, http://dx.doi.org/10.1680/geot.2003.53.7.655.

Mao, Z., Saint-André, L., Genet, M., Mine, F. X., Jourdan, C., Rey, H., Courbaud, B. & Stokes, A. (2012). Engineering ecological protection against landslides in diverse mountain forests: choosing cohesion models. *Ecol. Engng* **45**, 55–69.

McVay, M., Casper, R. & Shang, Te-I. (1995). Lateral response of three-row groups in loose to dense sands at 3D and 5D pile spacing. *J. Geotech. Engng* **121**, No. 5, 436–441.

McVay, M., Zhang, L., Molnit, T. & Lai, P. (1998). Centrifuge testing of large laterally loaded pile groups in sands. *J. Geotech. Geoenviron. Engng* **124**, No. 10, 1016–1026.

Mickovski, S. B., Hallett, P. D., Bransby, M. F., Davies, M. C. R., Sonnenberg, R. & Bengough, A. G. (2009). Mechanical reinforcement of soil by willow roots: impacts of root properties and root failure mechanism. *Soil Sci. Soc. Am. J.* **73**, No. 4, 1276–1285.

Mickovski, S. B., Stokes, A., van Beek, R., Ghestem, M. & Fourcaud, T. (2011). Mechanical reinforcement of soil by willow roots: impacts of root properties and root failure mechanism. *Ecol. Engng* **37**, No. 10, 1523–1532.

Nova-Roessig, L. & Sitar, N. (2006). Centrifuge model studies of the seismic response of reinforced soil slopes. *J. Geotech. Geoenviron. Engng* **132**, No. 3, 388–400.

Pollen, N. & Simon, A. (2005). Estimating the mechanical effects of riparian vegetation on stream bank stability using a fiber bundle model. *Water Resources Res.* **41**, No. 7, 1–11.

Randolph, M. F. (1981). The response of flexible piles to lateral loading. *Géotechnique.* **31**, No. 2, 247–259, http://dx.doi.org/10.1680/geot.1981.31.2.247.

Randolph, M. F. (2003). Science and empiricism in pile foundation design. *Géotechnique.* **53**, No. 10, 847–875, http://dx.doi.org/10.1680/geot.2003.53.10.847.

Reese, L. C. & Van Impe, W. (2011). *Single piles and pile groups under lateral loading*, 2nd edn. Boca Raton, FL, USA: CRC Press.

Reese, L. C., Cox, W. R. & Grubbs, B. R. (1974). Field testing of laterally loaded piles in sand. *Proceedings of the offshore technology conference*, Houston, TX, USA, pp. 459–472.

Rollins, K. M., Lane, J. D. & Gerber, T. M. (2005). Measured and computed lateral response of a pile group in sand. *J. Geotech. Geoenviron. Engng* **131**, No. 1, 103–114.

Schanz, T., Vermeer, A. & Bonnier, P. (1999). The hardening soil model: formulation and verification. In *Beyond 2000 in computational geotechnics 10 years of Plaxis* (ed. R. J. Brinkgreve), pp. 281–290. Rotterdam, the Netherlands: Balkema.

Sonnenberg, R. (2008). *Centrifuge modelling of root reinforced slopes*. PhD thesis, University of Dundee, Dundee, UK.

Sonnenberg, R., Bransby, M. F., Hallett, P. D., Bengough, A. G., Mickovski, S. B. & Davies, M. C. R. (2010). Centrifuge modelling of soil slopes reinforced with vegetation. *Can. Geotech. J.* **47**, No. 12, 1415–1430.

Sonnenberg, R., Bransby, M. F., Bengough, A. G., Hallett, P. D. & Davies, M. C. R. (2011). Centrifuge modelling of soil slopes containing model plant roots. *Can. Geotech. J.* **49**, No. 1, 1–17.

Timoshenko, S. P. & Goodier, J. N. (1970). *Theory of elasticity*, 3rd edn. Singapore: McGraw Hill.

Tiwari, R. C., Bhandary, N. P., Yatabe, R. & Bhat, D. R. (2013). New numerical scheme in the finite element method for evaluating the root-reinforcement effect on soil slope stability. *Géotechnique* **63**, No. 2, 129–139, http://dx.doi.org/10.1680/geot.11.P.039.

Van Beek, L. P. H., Wint, J., Cammeraat, L. H. & Edwards, J. P. (2005). Observation and simulation of root reinforcement on abandoned Mediterranean slopes. *Plant and Soil* **278**, No. 1–2, 55–74.

Waldron, L. J. (1977). The shear resistance of root-permeated homogeneous and stratified soil. *Soil Sci. Soc. Am. J.* **41**, No. 5, 843–849.

Warren, E., Smith, R. G. B., Apiolaza, L. A. & Walker, J. C. F. (2009). Effect of stocking on juvenile wood stiffness for three Eucalyptus species. *New Forests* **37**, No. 3, 241–250.

Wu, T. (2013). Root reinforcement of soil: review of analytical models, test results, and applications to design. *Can. Geotech. J.* **50**, No. 3, 259–274.

Yegian, M. & Wright, S. G. (1973). Lateral soil resistance displacement relationships for pile foundations in soft clays. *Proceedings of the offshore technology conference*, Houston, TX, USA, pp. 663–676.

Zeng, X. & Schofield, A. N. (1996). Design and performance of an equivalent-shear-beam container for earthquake centrifuge modelling. *Géotechnique.* **46**, No. 1, 83–102, http://dx.doi.org/10.1680/geot.1996.46.1.83.